Dalton Transactions

ROYAL SOCIETY OF CHEMISTRY

PAPER

View Article Online
View Journal | View Issue

Check for updates

Cite this: *Dalton Trans.*, 2024, **53**, 5676

Nickel, copper, and zinc dinuclear helicates: how do bulky groups influence their architecture?†

Sandra Fernández-Fariña, [b] Marcelino Maneiro, [b] Guillermo Zaragoza,[c] José M. Seco, [d] Rosa Pedrido *[a] and Ana M. González-Noya *[a]

Received 30th January 2024,
Accepted 26th February 2024

DOI: 10.1039/d4dt00279b

rsc.li/dalton

The ligand design factors that may influence the isolation of metallosupramolecular helicates or mesocates still deserve to be investigated. In this sense, dinuclear nickel(II), copper(II) and zinc(II) compounds were obtained by electrochemical synthesis using a family of five Schiff base ligands, H_2L^n (n = 1–5), derived from bisphenylmethane and functionalized with bulky *tert*-butyl groups in the periphery and ethyl groups in the spacer. Six of the new complexes were characterized by X-ray crystallography, thus demonstrating that the helicate structure is predominant in the solid state. ^{1}H NMR studies were performed for the zinc complexes to analyze if the helical architecture of the metal complexes is retained in solution. These studies reveal that the presence of a *tert*-butyl group in the *ortho* position with respect to the OH group is an essential factor identified for the existence of a helicate conformation in solution.

Introduction

The knowledge and understanding of how different elements and molecules combine through diverse self-assembly processes has led to the emergence of a new field called supramolecular chemistry.[1] Supramolecular chemistry is focused on the design and study of those systems formed by the spontaneous union of two or more components through the interaction of non-covalent bonds, for instance, hydrogen bonds, van der Waals forces or π–π interactions.[2–4] These interactions are often found in nature, such as in proteins or DNA, and are essential for the development of their main functions.[5]

Metal–ligand interactions are also important tools within the supramolecular chemistry field. Depending on the orientation of the parent ligand, a wide variety of metallosupramolecular architectures showing interesting properties and applications[5–7] can be obtained. Among them, helicates and mesocates have emerged as two of the most promising functional metallosupramolecular architectures. Helicates are formed by one or more organic ligands helically wrapped around a series of metal ions defining the axis of the helix.[1,8–10] In contrast, mesocates are formed by two or more ligands coordinated to metal ions without crossing each other.[11] Currently, in contrast to mesocates, helicates have been extensively studied. In this sense, a few reviews on helicates can be found in the literature.[10,12–15] Although the preparation of helicate/mesocate architectures is relatively simple, a single controlled route to achieving helicate *versus* mesocate has not yet been established. In recent years, some of the factors that govern the self-assembly processes of helicates and/or mesocates have been identified: the coordinative preferences of the metal ion, its size[16] and hard or soft characteristic,[17] the inner design of the organic ligand,[3,16,18–23] the temperature and the presence of anions.[24] It should be highlighted that understanding and controlling these factors are crucial because helicate/mesocate isomers may exhibit different biological behaviours.[25] Additionally, it has been found that the isolation of helicoidal or meso-helicoidal architectures can be controlled by intra- and intermolecular interactions that occur between the ligands.[26,27] In the literature there is a large variety of examples of helicoidal architectures derived from ligands whose formation is favoured by the existence of weak non-covalent π–π or CH···π interactions.[28–31] Along this line, it was found that the existence of non-covalent CH···π interactions favoured the helicate-type structure, contrary to expectations, since increasing the distance between the linking domains of the ligand should favour the mesocate conformation.[32]

[a]*Departamento de Química Inorgánica, Facultade de Química, Campus Vida, Universidade de Santiago de Compostela, Santiago de Compostela, Galicia, E-15782, Spain. E-mail: rosa.pedrido@usc.es, ana.gonzalez.noya@usc.es*
[b]*Departamento de Química Inorgánica, Facultade de Ciencias, Campus Terra, Universidade de Santiago de Compostela, E-27002 Lugo, Spain*
[c]*Unidade de Difracción de Raios X, Edificio CACTUS, Universidade de Santiago de Compostela, Campus Sur, Santiago de Compostela, Galicia, E-15782, Spain*
[d]*Departamento de Química Orgánica Facultade de Química, Campus Vida, Universidade de Santiago de Compostela, Santiago de Compostela, Galicia, E-15782, Spain*

†Electronic supplementary information (ESI) available: Detailed experimental procedures, compound characterization and synthetic and crystallographic data; Fig. S1–S14 and Tables S1–S8. CCDC 2321087–2321094. For ESI and crystallographic data in CIF or other electronic format see DOI: **https://doi.org/10.1039/d4dt00279b**

With this in mind, we have decided to delve deeper into the factors that influence both the metal ions and the ligand design for obtaining helical or meso-helical compounds. To achieve that, the coordination chemistry of a family of bisphenylmethane-derived Schiff base ligands (H_2L^n, Fig. 1) has been explored towards nickel(II), copper(II) and zinc(II) metal ions. Schiff base ligands[33] constitute one of the most used approaches for synthesizing helicates and mesocates, as they require cheap or easy-to-prepare starting materials and short preparation times.[15,19,34]

The long and semi-rigid bisphenylmethane-derived spacers were successfully employed by Hannon and co-workers in the parent ligands to prepare helicates and/or mesocates.[28,35–37] In fact, these pioneering works established that functionalization with ethyl groups in the aromatic rings of the spacer could foreseeably favour the formation of helicoidal species instead of mesocates.[37] In addition, different bisphenylmethane-derived ligands leading to helical-type species are found in the literature.[31,38–40]

Besides, the Schiff base branches in our series H_2L^n (Fig. 1) have been functionalized with *tert*-butyl groups in the salicyloyl groups (Fig. 1). We will modify the position of the *tert*-butyl group with respect to the hydroxy group (*para* for $\mathbf{H_2L^1}$ and $\mathbf{H_2L^4}$, and *ortho* for $\mathbf{H_2L^2}$ and $\mathbf{H_2L^5}$) and introduce a second *tert*-butyl group ($\mathbf{H_2L^3}$) to determine whether the position and number of bulky groups prevent and/or determine the formation of helicates or mesocates. The presence of the alkyl groups in the skeleton of these ligands could also improve the solubility of the species formed in apolar solvents and thus favour their crystallization.

Experimental section

Materials and methods

All solvents, *p*-toluenesulfonic acid, 4,4′-methylenedianiline, 4,4′-methylenebis(2,6-diethylaniline), 3-*tert*-butyl-2-hydroxybenzaldehyde, 5-*tert*-butyl-2-hydroxybenzaldehyde, 3,5-di-*tert*-butyl-2-hydroxybenzaldehyde and nickel, copper and zinc plates were purchased from commercial sources and were used without purification. Melting points were determined using a Buchi 560 instrument. Elemental analysis of compounds (C, N and H) was carried out on a Fisons EA model 1108 analyser. Infrared spectra were recorded from 4000 to 500 cm^{-1} on a Bruker FT-MIR spectrophotometer model VERTEX 70V in the solid state using KBr pellets. Mass spectra were obtained using Bruker Microtof spectrometers for the ESI^+ technique (electrospray ionization in positive mode) and Bruker Autoflex for the MALDI technique (matrix assisted laser desorption/ionization), both coupled to a time-of-flight (TOF) analyser. Room-temperature magnetic susceptibilities were measured using a digital measurement system MSB-MKI vibrating magnetometer. Tetrakis(isothiocyanato)cobaltate(II) was employed as a susceptibility standard. A Varian Inova 400 spectrometer was employed to record the ^1H NMR spectra operating at room temperature using acetone-d_6 as a deuterated solvent. Chemical shifts are reported as δ (in ppm).

Synthesis and characterization of the Schiff base ligands H_2L^n

The Schiff base ligands H_2L^n (n = 1–5) have been prepared by a condensation reaction between two equivalents of the corresponding hydroxyl-benzaldehyde functionalized with *tert*-butyl groups and one equivalent of the amine compound (Fig. S13†), following the same procedure previously reported for $\mathbf{H_2L^1}$ **1** and $\mathbf{H_2L^2}$ **2** ligands.[41] All the ligands have been fully characterized by melting point determination, elemental analysis, infrared spectroscopy, mass spectrometry and ^1H NMR spectroscopy techniques, as well as by X-ray diffraction in the cases where it was possible to obtain quality crystals.

$\mathbf{H_2L^3}$ 3. Yield: 1.38 g (87%); m.p.: 190–195 °C; elemental analysis: % theoretical ($C_{43}H_{54}N_2O_2$) C, 81.9; N, 4.4; H, 8.6; experimental C, 81.3; N, 4.4; H, 9.2; IR (cm^{-1}) ν: 3435 s (O–H), 2958 *vs.* (C–H), 1618 *vs.* (C=N), 1250 m (C–O), 820 w (CH_2); MALDI-TOF (m/z) 631.1 $[\mathbf{H_2L^3} + H]^+$; ^{1}H-NMR (400 MHz, acetone-d_6, δ (m, nH, Hx, J)): 13.88 (s, 2H, H_1), 8.90 (s, 2H, H_2), 7.50 (bs, J = 2.3 Hz, 2H, H_3), 7.46 (bs, J = 2.3 Hz, 2H, H_4), 7.31 (bs, 8H, H_5 + H_6), 4.08 (s, 2H, H_7), 1.47 (s, 18H, H_8), 1.33 (s, 18H, H_9).

$\mathbf{H_2L^4}$ 4. Yield: 0.405 g (81%); m.p.: 165–170 °C; elemental analysis: % theoretical ($C_{43}H_{54}N_2O_2$) C, 81.9; N, 4.4; H, 8.6; experimental C, 80.7; N, 4.3; H, 8.4; IR (cm^{-1}) ν: 3395 vw (O–H), 2963 s (C–H), 1628 *vs.* (C=N), 1265 s (C–O), 824 m (CH_2); ESI^+ (m/z) 631.4 $[\mathbf{H_2L^4} + H]^+$; ^{1}H-NMR (400 MHz, acetone-d_6, δ (m, nH, Hx, J)): 12.79 (s, 2H, H_1), 8.56 (s, 2H, H_2), 7.61 (d, J = 2.2 Hz, 2H, H_3), 7.52 (dd, J = 8.7, 2.4 Hz, 2H, H_4), 7.09 (s, 4H,

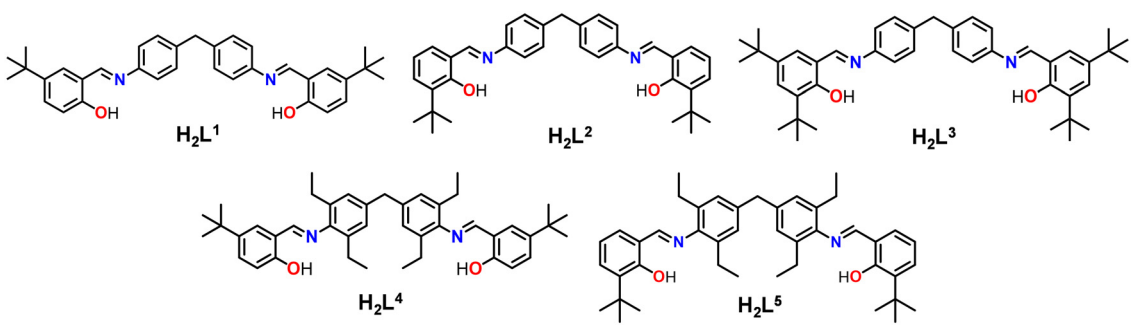

Fig. 1 Synthesized Schiff base ligands H_2L^n.

H_5), 6.94 (d, J = 8.7 Hz, 2H, H_6), 3.94 (s, 2H, H_7), 2.53 (q, J = 7.5 Hz, 8H, H_8), 1.47 (s, 18H, H_9); 1.12 (t, J = 7.5 Hz, 12H, H_{10}). By slow evaporation of the mother liquor during the synthesis of the ligand in ethanol, colourless prisms suitable for X-ray diffraction studies were obtained **H_2L^4 4***.

H_2L^5 5. Yield: 0.431 g (86%); m.p.: 110–115 °C; elemental analysis: % theoretical ($C_{43}H_{54}N_2O_2$) C, 81.9; N, 4.4; H, 8.6; experimental C, 79.8; N, 4.5; H, 8.9; IR (cm^{-1}) ν: 3433 vw (O–H), 2964 s (C–H), 1618 *vs.* (C═N), 1190 s (C–O), 750 m (CH_2); ESI$^+$ (m/z) 631.4 $[H_2L^5 + H]^+$; ^{1}H-NMR (400 MHz, acetone-d_6, δ (m, nH, Hx, J)): 13.82 (s, 2H, H_1), 8.54 (s, 2H, H_2), 7.45 (dd, J = 7.8, 1.2 Hz, 2H, H_3), 7.41 (dd, J = 7.8, 1.5 Hz, 2H, H_4), 7.11 (s, 4H, H_5), 6.93 (t, J = 7.8 Hz, 2H, H_6), 3.95 (s, 2H, H_7), 2.54 (c, J = 7.5 Hz, 8H, H_8), 1.47 (s, 18H, H_9); 1.13 (t, J = 7.5 Hz, 12H, H_{10}). By slow evaporation of the mother liquor during the synthesis of the ligand in ethanol, colourless prisms suitable for X-ray diffraction studies were obtained **H_2L^5 5***.

Synthesis and characterization of helicates

The electrochemical synthesis of nickel, copper, and zinc neutral helicates was performed using an electrochemical cell and a power supply to regulate the intensity (10 mA) and the potential (10–15 V) of the reaction.[41] The cell contains a solution of the Schiff base ligand in acetonitrile, along with a small quantity of tetraethylammonium perchlorate (10 mg) to act as a conductive electrolyte. The electrochemical reaction involves reduction of the ligand at the platinum cathode and oxidation of the metal anode. The electrochemical cell is depicted as follows:

$$\mathrm{Pt}(-)|\mathrm{H_2L}^n + \text{acetonitrile}|\mathrm{M}(+)$$

The proposed mechanism for the formation of the neutral helicates $[M_2(L)_2]$ involves two electrons per ligand, as shown below.

$$\text{Cathode}: \ 2\mathrm{H_2L}^n + 4\mathrm{e}^- \rightarrow 2(\mathrm{L}^n)^{2-} + 2\mathrm{H_2(g)}$$

$$\text{Anode}: \ 2\mathrm{M} \rightarrow 2\mathrm{M}^{2+} + 4\mathrm{e}^-$$

$$\text{Global}: \ 2(\mathrm{L}^n)^{2-} + 2\mathrm{M}^{2+} \rightarrow [\mathrm{M_2(L}^n)_2]$$

The main analytical and characterization data of the complexes are given below.

$[Ni_2(L^1)_2]\cdot H_2O$ 6. Yellow solid. Yield: 0.071 g (59%); m.p.: > 300 °C; E_f = 0.5 mol F^{-1}; elemental analysis: % theoretical ($C_{70}H_{74}N_4O_5Ni_2$) C, 72.0; N, 4.8; H, 6.4; experimental C, 70.9; N, 4.7; H, 6.1; IR (cm^{-1}) ν: 3435 s (O–H); 2958 m (C–H); 1620 *vs.* (C═N); 1261 m (C–O); 833 m (CH_2); MALDI-TOF (m/z): 1151.3 $[Ni_2(L^1)_2 + H]^+$, 1726.5 $[Ni_3(L^1)_3 + H]^+$; μ_{eff} = 3.1 B.M.

$[Ni_2(L^2)_2]\cdot H_2O$ 7. Orange solid. Yield: 0.069 g (58%); m.p.: > 300 °C; E_f = 0.5 mol F^{-1}; elemental analysis: % theoretical ($C_{70}H_{74}N_4O_5Ni_2$) C, 72.0; N, 4.8; H, 6.4; experimental C, 71.3; N, 4.7; H, 6.4; IR (cm^{-1}) ν: 3433 *vs.* (O–H); 2957 m (C–H); 1607 *vs.* (C═N); 1271 w (C–O); 752 m (CH_2); MALDI-TOF (m/z): 1151.5 $[Ni_2(L^2)_2 + H]^+$; μ_{eff} = 3.0 B.M. By slow evaporation of the mother liquor during the synthesis, brown crystals suitable for X-ray diffraction studies were obtained $[Ni_2(L^2)_2]\cdot CH_3CN$ 7*.

$[Ni_2(L^3)_2]$ 8. Orange solid. Yield: 0.064 g (59%); m.p.: decomposes at 230 °C; E_f = 0.5 mol F^{-1}; elemental analysis: % theoretical ($C_{86}H_{104}N_4O_4Ni_2$) C, 75.1; N, 4.1; H, 7.6; experimental C, 73.0; N, 3.9; H, 7.8; IR (cm^{-1}) ν: 2956 s (C–H); 1614 s (C═N); 1255 m (C–O); 837 w (CH_2); MALDI-TOF (m/z): 688.7 $[Ni(L^3) + H]^+$; μ_{eff} = 3.4 B. Recrystallization in dichloromethane yielded yellow prisms suitable for X-ray diffraction studies $[Ni_2(L^3)_2]\cdot 2CH_2Cl_2$ 8*.

$[Ni_2(L^4)_2]\cdot H_2O$ 9. Green solid. Yield: 0.062 g (54%); m.p.: 255 °C; E_f = 0.6 mol F^{-1}; elemental analysis: % theoretical ($C_{86}H_{106}N_4O_5Ni_2$) C, 74.1; N, 4.0; H, 7.7; experimental C, 72.6; N, 3.9; H, 7.5; IR (cm^{-1}) ν: 3442 m (O–H); 2963 s (C–H); 1618 *vs.* (C═N); 1267 m (C–O); 831 w (CH_2); MALDI-TOF (m/z): 1375.8 $[Ni_2(L^4)_2 + H]^+$; μ_{eff} = 3.2 B.M.

$[Ni_2(L^5)_2]$ 10. Brown solid. Yield: 0.065 g (59%); m.p.: 225 °C; E_f = 0.5 mol F^{-1}; elemental analysis: % theoretical ($C_{86}H_{104}N_4O_8Ni_2$) C, 75.1; N, 4.1; H, 7.6; experimental C, 74.3; N, 3.9; H, 7.3; IR (cm^{-1}) ν: 2967 s (C–H); 1605 s (C═N); 1269 w (C–O); 853 w (CH_2); MALDI-TOF (m/z): 1375.7 $[Ni_2(L^5)_2 + H]^+$; μ_{eff} = 3.3 B.M.

$[Cu_2(L^3)_2]\cdot H_2O$ 11. Brown solid. Yield: 0.075 g (65%); m.p.: 200 °C; E_f = 0.5 mol F^{-1}; elemental analysis: % theoretical ($C_{86}H_{106}N_4O_5Cu_2$) C, 73.6; N, 4.0; H, 7.6; experimental C, 74.3; N, 3.9; H, 7.4; IR (KBr, cm^{-1}): ν = (O–H) 3444 (d), (C–H) 2954 (f), (C═N) 1614 (f), (C–O) 1255 (m), (CH_2) 833 (d); MALDI-TOF (m/z) 694.5 $[Cu(L^3) + H]^+$, 1386.9 $[Cu_2(L^3)_2 + H]^+$; μ_{eff} = 1.7 B.M. By slow evaporation of the mother liquor during the synthesis, brown crystals suitable for X-ray diffraction studies were obtained $[Cu_2(L^3)_2]\cdot 2CH_3CN$ 11*.

$[Cu_2(L^4)_2]$ 12. Brown solid. Yield: 0.059 g (51%); m.p.: 260 °C; E_f = 0.5 mol F^{-1}; elemental analysis: % theoretical ($C_{86}H_{104}N_4O_4Cu_2$) C, 71.4; N, 3.9; H, 7.8; experimental C, 68.8; N, 3.7; H, 7.5; IR (KBr, cm^{-1}): ν = (C–H) 2963 (m), (C═N) 1618 (m), (C–O) 1267 (d), (CH_2) 835 (d); MALDI-TOF (m/z) 691.5 $[Cu(L^4) + H]^+$, 1386.9 $[Cu_2(L^4)_2 + H]^+$; μ_{eff} = 1.9 B.M.

$[Cu_2(L^5)_2]\cdot H_2O$ 13. Brown solid. Yield: 0.074 g (67%); m.p.: 220 °C; E_f = 0.5 mol F^{-1}; elemental analysis: % theoretical ($C_{86}H_{104}N_4O_4Cu_2$) C, 71.4; N, 3.9; H, 7.8; experimental C, 72.3; N, 3.9; H, 7.3; IR (KBr, cm^{-1}): ν = (C–H) 2963 (m), (C═N) 1603 (mf), (C–O) 1184 (m), (CH_2) 750 (d); MALDI-TOF (m/z) 691.3 $[Cu(L^5) + H]^+$, 1386.6 $[Cu_2(L^5)_2 + H]^+$. μ_{eff} = 1.8 B.M. By slow evaporation of the mother liquor during the synthesis, brown crystals suitable for X-ray diffraction studies were obtained $[Cu_2(L^5)_2]\cdot 2CH_3CN$ 13*.

$[Zn_2(L^1)_2]$ 14. Yellow solid. Yield: 0.071 g (59%); m.p.: > 300 °C; E_f = 0.5 mol F^{-1}; elemental analysis: % theoretical ($C_{70}H_{72}N_4O_4Zn_2$) C, 72.2; N, 4.8; H, 6.2; experimental C, 70.1; N, 4.5; H, 6.6; IR (cm^{-1}) ν: 3435 s (O–H); 2959 m (C–H); 1618 s (C═N); 1263 m (C–O); 833 m (CH_2); MALDI-TOF (m/z): 581.9 $[Zn(L^1) - H]^+$, 1165.3 $[Zn_2(L^1)_2 + H]^+$, 1745.4 $[Zn_3(L^1)_3 + H]^+$; ^{1}H-NMR (400 MHz, acetone-d_6) δ/ppm: 8.63 (s_b, 2H, H_2), 7.50 (s_b, 2H, H_{Ar}), 7.39 (s_b, 2H, H_{Ar}), 6.94 (s_b, 8H, H_{Ar}), 6.84 (s_b, 2H, H_{Ar}), 3.87 (s, H_8), 1.32 (s_b, 18H, H_9). Recrystallization in a mixture of dichloromethane : methanol (1 : 1) yielded yellow prisms suitable for X-ray diffraction studies $[Zn_2(L^1)_2]\cdot 2.8CH_3OH$ 14*.

$[Zn_2(L^2)_2]$ 15. Yellow solid. Yield: 0.065 g (58%); m.p.: > 300 °C; E_f = 0.5 mol F^{-1}; elemental analysis: % theoretical ($C_{70}H_{72}N_4O_4Zn_2$) C, 72.2; N, 4.8; H, 6.2; experimental C, 69.1; N, 5.0; H, 6.0; IR (cm^{-1}) ν: 2955 w (C–H); 1614 w (C=N); 1292 vw (C–O); 752 w (CH_2); MALDI-TOF (*m*/*z*): 581.9 $[Zn(L^2) - H]^+$, 1165.3 $[Zn_2(L^2)_2 + H]^+$, 1745.4 $[Zn_3(L^2)_3 + H]^+$; ^{1}H-NMR (400 MHz, acetone-d_6) δ/ppm: 8.59 (s, 2H, H_2), 7.42 (m, H_{Ar}), 7.28 (d, 2H, H_{Ar}), 6.94 (s, 8H, $H_5 + H_6$), 6.63 (t, 2H, H_7), 3.87 (s, H_8), 1.48 (s, 18H, H_9).

$[Zn_2(L^3)_2]$ 16. Yellow solid. Yield: 0.071 g (72%); m.p.: 270 °C; E_f = 0.5 mol F^{-1}; elemental analysis: % theoretical ($C_{86}H_{112}N_4O_8Zn_2$) C, 70.7; N, 3.8; H, 7.7; experimental C, 68.6; N, 3.6; H, 7.3; IR (cm^{-1}) ν: 3442 m (O–H); 2958 m (C–H); 1616 s (C=N); 1253 m (C–O); 789 w (CH_2); MALDI-TOF (*m*/*z*): 1389.0 $[Zn_2(L^3)_2 + H]^+$; ^{1}H-NMR (400 MHz, acetone-d_6) δ/ppm: 8.60 (s, 2H, H_2), 7.56 (s_a, 2H, H_3), 7.26 (s_a, 2H, H_4), 6.94 (s_a, 8H, H_{Ar}), 3.87 (s, H_5), 1.50 (s, 18H, H_6), 1.33 (s, 18H, H_7).

$[Zn_2(L^4)_2]$ 17. Yellow solid. Yield: 0.060 g (54%); m.p.: 265 °C; E_f = 0.6 mol F^{-1}; elemental analysis: % theoretical ($C_{86}H_{104}N_4O_4Zn_2$) C, 74.4; N, 4.0; H, 7.5; experimental C, 73.1; N, 3.9; H, 7.3; IR (cm^{-1}) ν: 2963 s (C–H); 1622 *vs.* (C=N); 1260 m (C–O); 833 w (CH_2); MALDI-TOF (*m*/*z*): 1389.6 $[Zn_2(L^4)_2 + H]^+$; ^{1}H-NMR (400 MHz, acetone-d_6) δ/ppm: 8.25 (s, 2H, H_2), 7.61–6.66 (m, 10H, H_{Ar}), 3.99 (s, H_7), 2.53 (c, 8H, H_8), 1.27 (m, 18H, H_9), 0.77 (t, 12H, H_{10}).

$[Zn_2(L^5)_2]\cdot H_2O$ 18. Yellow solid. Yield: 0.052 g (46%); m.p.: 225 °C; E_f = 0.7 mol F^{-1}; elemental analysis: % theoretical ($C_{86}H_{106}N_4O_5Zn_2$) C, 73.4; N, 4.0; H, 7.6; experimental C, 73.1; N, 3.8; H, 7.4; IR (cm^{-1}) ν: 3442 m (O–H); 2965 s (C–H); 1607 *vs.* (C=N); 1180 m (C–O); 750 m (CH_2); MALDI-TOF (*m*/*z*): 1388.6 $[Zn_2(L^5)_2 + H]^+$; ^{1}H-NMR (400 MHz, acetone-d_6) δ/ppm: 8.22 (s, 2H, H_2), 7.46–7.36 (m, H_{Ar}), 7.20 (d, H_{Ar}), 7.15–7.13 (m, H_{Ar}), 6.69 (s_a, H_{Ar}), 6.55 (t, 2H, H_6), 4.01 (s, H_7), 2.54 (c, H_8), 1.44 (s, H_9), 0.84 (t, H_{10}). By slow evaporation of the mother liquor during the synthesis, brown crystals suitable for X-ray diffraction studies were obtained $[Zn_2(L^5)_2]\cdot 2CH_3CN$ **18***.

Crystallographic data collection

Crystallographic data for ligands **H_2L^4 4*** and **H_2L^5 5*** and compounds **7***, **8***, **11***, **13***, **14*** and **18*** were collected at 100 K on a Bruker D8 VENTURE diffractometer equipped with a CCD detector, using a MoK(α) graphite monochromator (λ = 0.71073 Å). The data were treated using APPEX3v2018.7-2 software for all compounds, except for complex **8*** and **11***, which were treated using APPEX2 (Bruker AXS). In all cases, an absorption correction (SADABS)[42] was applied to the measured reflections. The **H_2L^5** structure was solved using SHELXT 2014/5,[43] while the remaining structures were solved with SHELXT2018/2.2. All structures were refined using SHELXL2018/3,[44] with the exception of the **11*** structure, which was refined using SHELXL2016/6.[43] Hydrogen atoms were included in the model at geometrically calculated and refined positions. The images included in this chapter were prepared using Mercury.[45] CCDC 2321087–2321094† contain the supplementary crystallographic data for the compounds.

Results and discussion

Schiff base ligands H_2L^n

The family of Schiff base ligands named H_2L^n (n = 1–5, Fig. 1) is potentially dianionic with two bidentate [NO] domains separated by a semi-rigid aromatic spacer. The ligands were fully characterized using a wide variety of techniques, as detailed in the Experimental section and in Fig. S1–S3 and Tables S1 and S2, (ESI).†

The study of the ligand crystal structures is relevant since it allows us to explore the conformational changes that should be undergone to coordinate to the metal ions. Previous studies showed that the presence of a large spacer determined that each of the [NO] linker domains of the ligand coordinated to different metal ions, giving rise to dinuclear helicoidal or meso-helicoidal structures.[46]

Quality crystals valid for X-ray diffraction studies of ligands **H_2L^4 4*** (Fig. 2) and **H_2L^5 5*** (Fig. 3) were obtained by slow evaporation of the ethanol mother liquors during the synthesis. Due to the similarity of their structures, both will be discussed together below.

The structures show discrete molecules crystallizing in the triclinic $P\bar{1}$ system. In both ligands the two branches exhibit an *E* configuration with respect to the imine bonds and a *syn*-type conformation, with respect to the spacer, with the two ligand branches oriented toward the same side. This conformation is achieved by the establishment of strong intramolecular hydrogen bonds[47] involving the imine nitrogen of each ligand branch and the phenol group (**H_2L^4 4***: O2–H20···N2 2.574 Å, O1–H10···N1 2.615 Å and **H_2L^5 5***: O2–H20···N1 2.586 Å, O1–H10···N2 2.565 Å). These interactions are different in the two ligands due to the opposite orientation adopted by the phenol ring as a consequence of the position of the *tert*-butyl group (*ortho* or *para*). In the case of an *ortho*

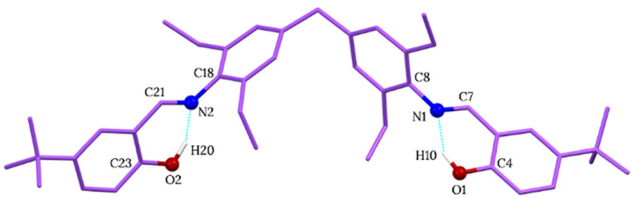

Fig. 2 Stick representation of the ligand **H_2L^4 4*** showing the *syn* configuration of its branches and the intramolecular hydrogen bonds.

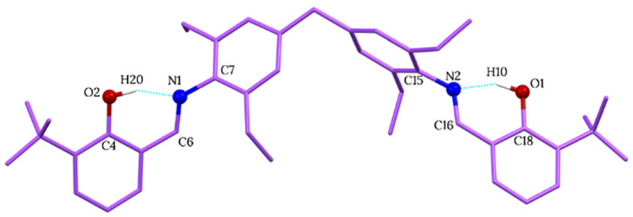

Fig. 3 Stick representation of the ligand **H_2L^5 5*** showing the *syn* configuration of its branches and the intramolecular hydrogen bonds.

substitution a rotation around the C=N bond is required to avoid unfavourable steric hindrance. The imine and phenol distances are in the usual range found in Schiff base ligands.[48,49]

Assembly of nickel(II), copper(II) and zinc(II) complexes

The next step was the preparation of the nickel, copper and zinc derived complexes with the ligands of the series H_2L^n. It is well known that metal ions would have their own coordinative preferences and different affinities to donor atoms, so the use of metal ions with different electronic configurations could lead to distinct metallosupramolecular structures.

The Cu^{2+} metal ion is a d^9 system that could exhibit different coordination geometries: square-planar or tetrahedral (four-coordinate), square pyramidal or trigonal bipyramidal (five-coordinate) or octahedral (six-coordinate). It is important to mention that the Cu(II) complexes derived from the ligands **H_2L^1** and **H_2L^2** were previously reported by us.[41] Both complexes were found to be similar tetracoordinated helicates $[Cu_2(L^{1|2})_2]\cdot x CH_3CN$ showing a distorted tetrahedral environment. In that work we observed that the position of the bulky *t*-butyl groups influenced the intermolecular Cu–Cu distance in the extended structures and their magnetic behaviour.

Our study was completed with Ni^{2+}, whose electronic configuration is d^8. The preferential coordination spheres of Ni^{2+} are six-coordinate (octahedral geometry)[19,50] or four-coordinate complexes with planar-square if the ligand-field is strong.[51] However, there are also some examples of tetrahedral geometries.[52] We have also chosen the softer acid Zn^{2+} ion, a d^{10} system whose geometrical preferences are more variable: octahedral (six-coordinate),[53] pentacoordinate with a square-based pyramidal geometry,[54,55] or the most common type, the tetrahedral geometry (four-coordinate).[16,54]

The neutral nickel, copper and zinc complexes derived from the Schiff base ligand series H_2L^n were prepared using an electrochemical methodology.[41] The isolated complexes are powdery solids stable to light and air. Both analytical and spectroscopic data allow us to propose dinuclear stoichiometry $[M_2(L^n)_2]$ for the complexes, with the ligands being bound to the metal ions in their dianionic $[L^n]^{2-}$ form. The IR spectra of the complexes exhibit some shifting in the ν(C=N) and ν(C–O) bands, thus indicating that the ligand coordinates to the metal ion *via* the imine nitrogen and phenolic oxygen atoms. The dinuclear nature of these complexes was additionally confirmed by MALDI-TOF (+) mass spectrometry experiments as peaks corresponding to the dinuclear fragments $[M_2(L^n)_2 + H]^+$ were observed (Fig. S4–S8†).

X-ray diffraction studies

The X-ray diffraction technique allowed us to analyse whether the number and position of the bulky groups of the ligands and the nature and coordinative preferences of the metal ion influence the final architecture of the complexes. Slow evaporation of the mother liquors during the synthesis of **7**, **11**, **13** and **18**, and recrystallization in dichloromethane (solid **8**) or dichloromethane : methanol (solid **14**) allowed us to obtain valid crystals for X-ray diffraction studies.

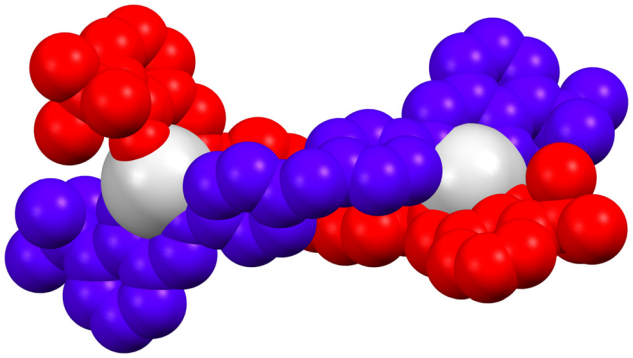

Fig. 4 Spacefill representation of the $[Ni_2(L^2)_2]\cdot CH_3CN$ **7*** complex, showing the helicoidal structure common to all the complexes studied by X-ray diffraction.

All the structures show four-coordinate dinuclear neutral helicate-type architecture (Fig. 4) formed by two strands of the dianionic ligand $[L^n]^{2-}$, which cross-coordinate around the two M(II) ions [M = Ni, Cu, and Zn].

Specifically, the structures revealed the formation of dinuclear neutral helicates $[Ni_2(L^2)_2]\cdot CH_3CN$ **7*** (Fig. 5), $[Ni_2(L^3)_2]\cdot 2CH_2Cl_2$ **8*** (Fig. 6), $[Cu_2(L^3)_2]\cdot 2CH_3CN$ **11*** (Fig. 7), $[Cu_2(L^5)_2]\cdot 3CH_3CN$ **13*** (Fig. 8), $[Zn_2(L^1)_2]\cdot 2.8CH_3OH$ **14*** (Fig. 9) and $[Zn_2(L^5)_2]\cdot 2CH_3CN$ **18*** (Fig. 10). Tables S3–S8† summarize the most relevant distances and angles.

The six crystal structures are similar so, in order to avoid repetitive descriptions, we will only describe in detail the zinc complex $[Zn_2(L^1)_2]\cdot 2.8CH_3OH$ **14*** (Fig. 9), highlighting only some structural facts that could be attributed to the substitution in the remaining complexes.

The molecular structure of **14*** (Fig. 9) shows a non-centrosymmetric dinuclear neutral Zn^{2+} complex. The two **H_2L^1** ligands are helically arranged around the two Zn^{2+} ions, so these metal centres have the same absolute configuration. The two enantiomers are present in the crystal cell as a racemate. The Schiff base ligands act in such a way that each of their bidentate [NO] branches coordinate to a different metal ion

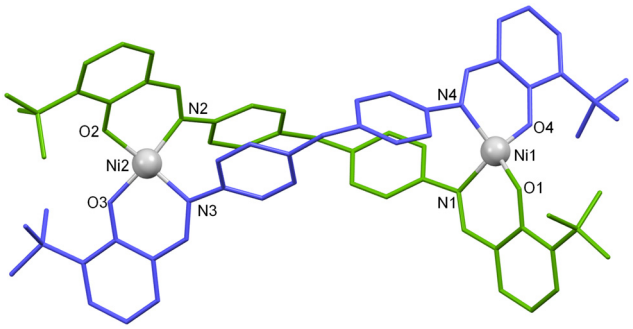

Fig. 5 Crystal structure of the nickel(II) helicate $[Ni_2(L^2)_2]\cdot CH_3CN$ **7***. Solvent molecules and hydrogen atoms have been omitted for clarity.

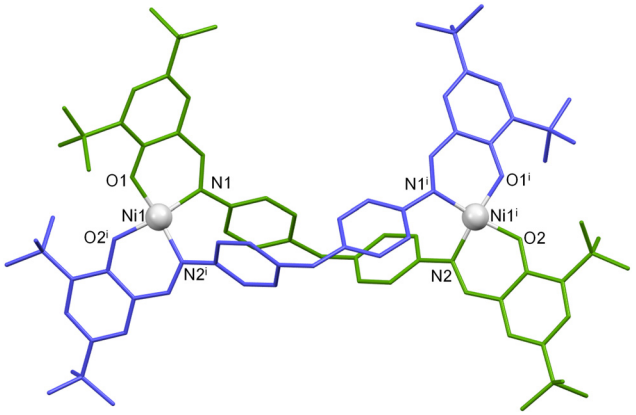

Fig. 6 Crystal structure of the nickel(II) helicate $[Ni_2(L^3)_2]\cdot 2CH_2Cl_2$ **8***. Solvent molecules and hydrogen atoms have been omitted for clarity.

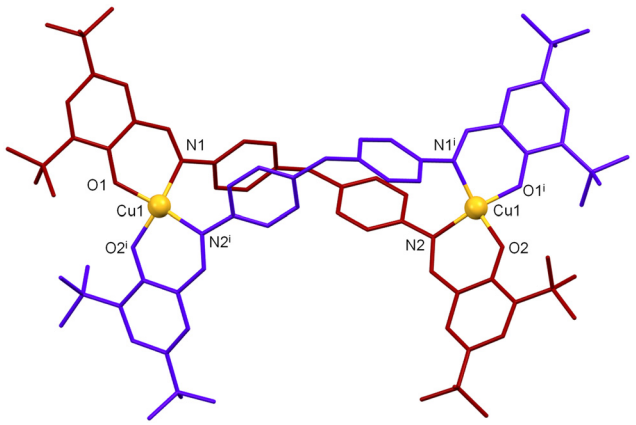

Fig. 7 Crystal structure of the copper(II) helicate $[Cu_2(L^3)_2]\cdot 2CH_3CN$ **11***. Solvent molecules and hydrogen atoms have been omitted for clarity.

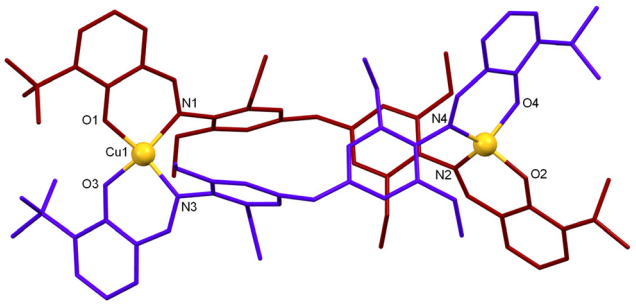

Fig. 8 Crystal structure of the copper(II) helicate $[Cu_2(L^5)_2]\cdot 3CH_3CN$ **13***. Solvent molecules and hydrogen atoms have been omitted for clarity.

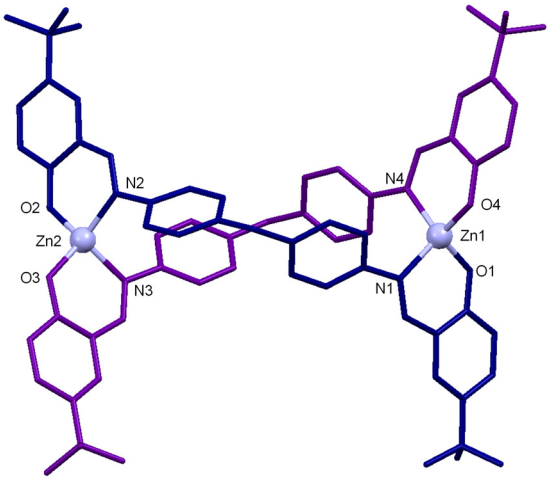

Fig. 9 Crystal structure of the zinc(II) helicate $[Zn_2(L^1)_2]\cdot 2.8CH_3OH$ **14***. Solvent molecules and hydrogen atoms have been omitted for clarity.

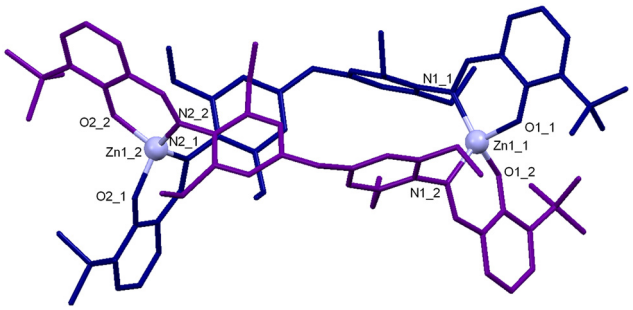

Fig. 10 Crystal structure of the zinc(II) helicate $[Zn_2(L^5)_2]\cdot 2CH_3CN$ **18***. Solvent molecules and hydrogen atoms have been omitted for clarity.

giving rise to a distorted tetrahedral geometry [$\neq 109.5^0$]. The O–M–N bond angles clearly show the distortion of the tetrahedral geometry (Table S7†). The main bond distances Zn–O and Zn–N are in the expected ranges for complexes derived from Schiff base ligands with phenol groups[56] with the Zn–O distance being slightly shorter than Zn–N distance (Table S7†). The intermetallic distance Zn⋯Zn (11.639 Å) is similar to the distance between the zinc ions in dinuclear helicoidal compounds and does not deserve further comments.[56]

On the other hand, hydrogen bonds are established between the O3 and O4 phenolic oxygens of the helicate ligands and two methanol molecules. In line with this, one of the solvent molecules forms a hydrogen bond with an adjacent methanol molecule [O6–H6⋯O3 2.74 Å, O5–H5⋯O4 2.76 Å and O6–H6⋯O7 2.74 Å] (Fig. S9†). Additionally, the existence of eight aromatic rings in each helicate makes it necessary to explore aromatic π–π or CH⋯π stacking interactions. Thus, there are weak π–π interactions between the aromatic rings of the two ligands that contribute to the stabilization of the helicoidal structure [the distance between centroids: 4.48 Å and 4.63 Å] (Fig. S9†).

In the case of the crystal lattice of $[Zn_2(L^1)_2]\cdot 2.8CH_3OH$ **14*** (Fig. 11), intermolecular π–π interactions are observed between the aromatic rings of the spacer of adjacent helicates (a centroid–centroid distance of 3.95 Å), with these interactions being stronger than the intramolecular ones (centroid to centroid distances: 4.2 and 4.6 Å).[57] Additionally, these inter-

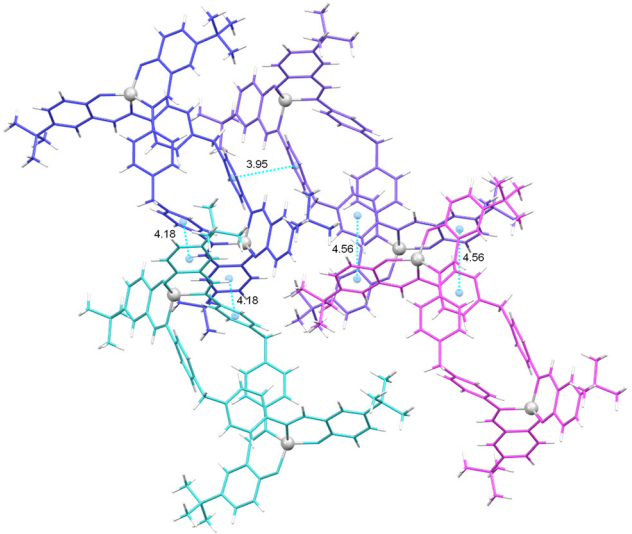

Fig. 11 Intermolecular π-stacking interactions in the crystal lattice of the complex $[Zn_2(L^1)_2]\cdot 2.8CH_3OH$ **14***.

actions are observed between one of the phenyl rings of the spacer and the aromatic ring of a linker domain (centroid–centroid distances of 3.59 and 3.44 Å).

In addition, CH···π interactions between the aromatic ring of one of the ligand branches and one of the *tert*-butyl substituents of the adjacent helicate can be observed in the crystalline packing of $[Zn_2(L^1)_2]\cdot 2.8CH_3OH$ **14***, (Fig. S10†).

It should be noted that the six helicoidal structures studied exhibit similar packing patterns to the **14*** helicate, except in the case of the $[Zn_2(L^5)_2]\cdot 2CH_3CN$ **18*** helicate (Fig. 10), where the stacking distances are much longer.

Additionally, as can be seen in Fig. S11–S14†, the complexes with *tert*-butyl groups in the *ortho* position to the phenol groups (**7***, **8***, **11***, **13***, and **18***) exhibit hydrogen bonds between the CH_3 of the *tert*-butyl groups and the phenolic oxygens. Additionally, the crystal structure derived from the $\mathbf{H_2L^5}$ ligand functionalized with ethyl groups on the spacer exhibits CH···π interactions between the ethyl groups and the aromatic rings of the adjacent ligand spacer (Fig. S13 and S14†).

The obtainment of dinuclear helicates in all these cases shows that the position and/or the number of bulky groups in the ligands does not affect the type of structure isolated, but it does affect the microstructure of the helicates.

Our results demonstrated that the functionalization of the ligands with ethyl substituents in the spacer ($\mathbf{H_2L4}$ and $\mathbf{H_2L^5}$) generates new intramolecular non-covalent CH···π interactions between the CH_2 of the ethyl groups and the aromatic rings of the spacer of the adjacent ligand, which could additionally favour the helicoidal conformation in the compounds.

Furthermore, the results demonstrate that the use of metal ions with different natures (Cu^{2+}, Ni^{2+} and Zn^{2+}) does not affect the arrangement of the ligands around the metal centres. In all cases, helicate architectures were achieved, indicating that the variation from Cu^{2+} to Ni^{2+} to a similar-sized metal ion Zn^{2+}, with no ligand-field stabilization energy, does not affect the macrostructure of the compounds.

If we check the coordination kernels in the two pairs of Ni(II), Cu(II) and Zn(II) helicates we can see that the Zn(II) helicates show a distorted tetrahedral geometry in both cases (**14***: τZn1 = 0.85, τZn2 = 0.76, Table S7;† **18***: τZn1 = 0.82, Table S8†), and the metal ions in the Cu(II) helicates exhibit intermediate τ_4 values (**11***: τCu1 = 0.43; **13***: τCu1 = 0.58, τCu2 = 0.42).[58] However, in the case of the Ni(II) helicate $[Ni_2(L^2)_2]\cdot CH_3CN$ **7***, this exhibits a distorted tetrahedral geometry around one of the nickel ions (Ni1) and a distorted square-planar geometry around the second metal ion (Table S3,† τNi1 = 0.76; τNi2 = 0.30) whereas a distorted square-planar environment around both Ni^{2+} metal ions was found in the case of $[Ni_2(L^3)_2]\cdot 2CH_2Cl_2$ **8*** (Table S4,† τNi1 = 0.28). In this case, the presence of one ($\mathbf{H_2L^2}$) or two *tert*-butyl groups ($\mathbf{H_2L^3}$) in the periphery of the ligands does affect the microstructure of the nickel complexes obtained.

^{1}H NMR studies

Hannon and co-workers[37] have a wide experience in the preparation of helicate/mesocate complexes with bisphenylmethane derived ligands. In these studies, they stated that a careful analysis of the ^{1}H NMR spectrum in the aliphatic region may be indicative of the exclusive presence of the mesocate and helicate conformations (Fig. 12) in solution, or the coexistence of both forms.

In this sense, they concluded that if the ligand spacer is not functionalised with alkyl substituents in the phenyl rings, a mixture of helicate–mesocate is shown, whereas when adding bulky groups (ethyl and methyl) to the ligand spacer, the mesocate architecture is precluded. This could be explained by the ligand twisting induced by the alkyl groups and also by the establishment of new CH···π intermolecular interactions which favour the helicate-type architecture (dinuclear and trinuclear with Me, and dinuclear with Et).

What happens if we also introduce bulky groups in the ligand branches? Trying to go a step further we studied the aliphatic methylene region for the series of the zinc complexes **14**, **15**, **16**, **17** and **18** in order to explore whether the helical structure observed in the solid state is maintained in solution.

The zinc complex **14** $[Zn_2(L^1)_2]$ derived from the ligand with the *para tert*-butyl group position shows a central singlet signal corresponding to the helicate-type conformation and four additional satellite signals that could correspond to mesocate species (Fig. 13), thus confirming that both species co-exist in solution. Therefore, the presence of an external *tert*-butyl group together with the non-substituted spacer does not tip

Fig. 12 Helicate (left) and mesocate (right) conformations.

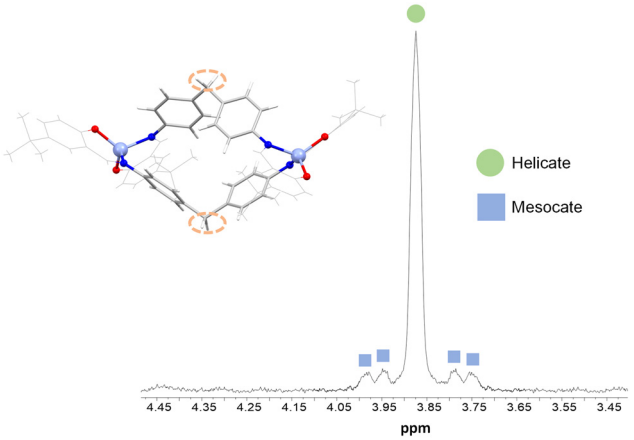

Fig. 13 ^{1}H NMR spectrum of the CH_2 group aliphatic region of $[Zn_2(L^1)_2]$ **14** (400 MHz, r.t., acetone-d_6).

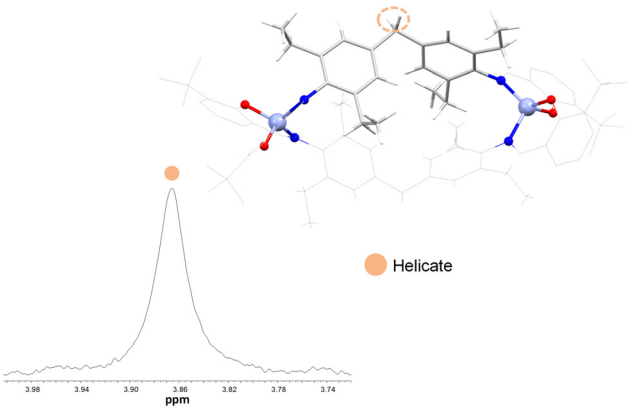

Fig. 14 ^{1}H NMR spectrum of the CH_2 group aliphatic region of $[Zn_2(L^5)_2]$ **18** (400 MHz, r.t., acetone-d_6).

the balance towards the mesocate or helicate species that co-exist in solution.

In contrast, the zinc complexes **15**, **16**, **17** and **18** show one singlet, thus indicating the exclusive presence of the helicate species in solution only (Fig. 14). These experimental observations indicate that in the absence of bulky groups in the spacer, the equilibrium of helicate/mesocate is displaced to helicate after functionalization of the external rings with a *tert* butyl group in the *ortho* position to the phenol.

Likewise, in the case of the zinc complexes derived from the ligands functionalised with the ethyl groups in the spacer rings, $[Zn_2(L^4)_2]$ **17** and $[Zn_2(L^5)_2]$ **18**, the helicate-type structure is also confirmed by the appearance of four signals corresponding to diastereotopic ethyl CH_2 protons (Fig. 15).

Thus, two of the signals appear at low field with respect to the free ligand and the remaining two signals appear at high

Table 1 Summary of the deduced helix of the meso-helical nature of the Zn(II) compounds **14–18** from ^{1}H NMR spectroscopy

Complex	Species	Spacer rings	Salicyloyl rings
14	Hel/Mes	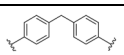	
15	Hel	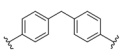	
16	Hel	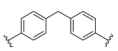	
17	Hel	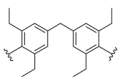	
18	Hel	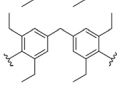	

Hel = Helicate; Mes = Mesocate.

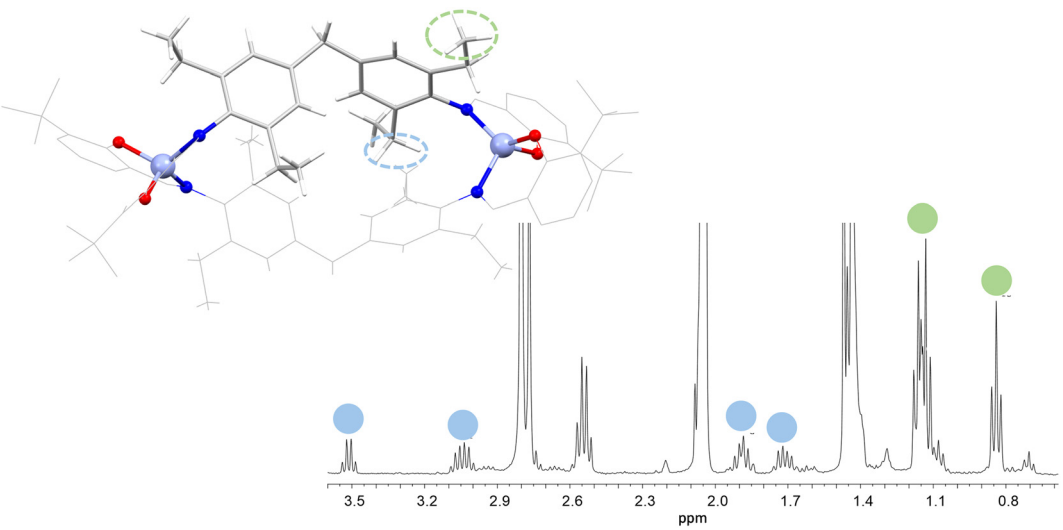

Fig. 15 ^{1}H NMR spectrum of the aliphatic region of $[Zn_2(L^5)_2]$ **18** (400 MHz, r.t., acetone-d_6).

field. In addition, two signals corresponding to the CH_3 of the ethyl groups are observed, one of which appears unshielded with respect to the free ligand due to the existence of π-stacking interactions along the crystal lattice.[37]

Therefore, the results of these NMR studies allow us to deduce that the driving factor determining the existence in solution of helicate or a helicate–mesocate mixture does not reside exclusively in the spacer, as the introduction of an *ortho* bulky group on the external surface of the helicate displaces the equilibrium of helicate–mesocate towards the helicate (Fig. 14 and Table 1). However, the introduction of ethyl groups in the ligand spacer still sterically favours the formation of helicates, independently of the presence of bulky groups in the periphery of the complex (Fig. 15 and Table 1).

Conclusions

Dinuclear nickel(II), copper(II) and zinc(II) complexes were isolated using an electrochemical methodology from a family of five Schiff base ligands derived from bisphenylmethane and functionalized with bulky *tert*-butyl groups. The introduction of bulky groups on both the spacer and ligand branches favours the formation of dinuclear helicates. From the six crystal structures reported in this work, we can conclude that small modifications of the ligands do not affect the macrostructure of the compounds, all of them being helicates. However, the microstructure, *e.g.*, the metal ion environment, could be altered in some cases. Besides, the introduction of ethyl substituents in the spacer provides new intramolecular interactions that stabilize the helicate-type architecture of the compounds. Furthermore, the ^{1}H NMR study reveals that the presence of the *tert*-butyl group in the *ortho* position with respect to the OH group is essential for the maintenance of the helicate conformation in solution.

Author contributions

The manuscript was written through the contributions of all authors. All authors have given approval to the final version of the manuscript.

Conflicts of interest

There are no conflicts to declare.

Acknowledgements

This research was funded by the following FEDER co-funded grants: Consellería de Cultura, Educación e Ordenación Universitaria, Xunta de Galicia GRC GI-1584 (ED431C 2023/02), MetalBIONetwork (ED431D2017/01), and Ministerio de Ciencia e Innovación, Project PID2021-127531NB-I00 (AEI/10.13039/501100011033/FEDER/UE).

References

1 J.-M. Lehn, *Angew. Chem., Int. Ed. Engl.*, 1988, **27**, 89–112.
2 M. Albrecht, M. Fiege and O. Osetska, *Coord. Chem. Rev.*, 2008, **252**, 812–824.
3 J. M. Lehn, *Chem. Soc. Rev.*, 2007, **36**, 151–160.
4 G. F. Swiegers and T. J. Malefetse, *Chem. Rev.*, 2000, **100**, 3483–3537.
5 H. Sepehrpour, W. Fu, Y. Sun and P. J. Stang, *J. Am. Chem. Soc.*, 2019, **141**, 14005–14020.
6 E. Chinnaraja, R. Arunachalam, E. Suresh, S. K. Sen, R. Natarajan and P. S. Subramanian, *Inorg. Chem.*, 2019, **58**, 4465–4479.
7 V. Martínez-Agramunt and E. Peris, *Inorg. Chem.*, 2019, **58**, 11836–11842.
8 J. M. Lehn, A. Rigault, J. Siegel, J. Harrowfield, B. Chevrier and D. Moras, *Proc. Natl. Acad. Sci. U. S. A.*, 1987, **84**, 2565–2569.
9 C. T. McTernan, T. K. Ronson and J. R. Nitschke, *J. Am. Chem. Soc.*, 2021, **143**, 664–670.
10 C. Piguet, G. Bernardinelli and G. Hopfgartner, *Chem. Rev.*, 1997, **97**, 2005–2062.
11 S. Fernández-Fariña, M. Martínez-Calvo, M. Maneiro, J. M. Seco, G. Zaragoza, A. M. González-Noya and R. Pedrido, *Inorg. Chem.*, 2022, **61**, 14121–14130.
12 H. Miyake and H. Tsukube, *Chem. Soc. Rev.*, 2012, **41**, 6977–6991.
13 M. Albrecht, X. Chen and D. Van Craen, *Chem. – Eur. J.*, 2019, **25**, 4265–4273.
14 J. L. Greenfield and J. R. Nitschke, *Acc. Chem. Res.*, 2022, **55**, 391–401.
15 M. Albrecht, *Chem. Rev.*, 2001, **101**, 3457–3497.
16 M. J. Romero, M. Martínez-Calvo, M. Maneiro, G. Zaragoza, R. Pedrido and A. M. González-Noya, *Inorg. Chem.*, 2019, **58**, 881–889.
17 T. L. Ho, *Chem. Rev.*, 1975, **75**, 1–20.
18 J. M. Lehn, *Eur. Rev.*, 2009, **17**, 263–280.
19 A. A. Escuer, J. Mayans, L. Di Bari, M. Font-, L. Arrico and F. Zinna, *Chem. – Eur. J.*, 2018, **24**, 7653–7663.
20 N. Wu, C. F. C. Melan, K. A. Stevenson, O. Fleischel, H. Guo, F. Habib, R. J. Holmberg, M. Murugesu, N. J. Mosey, H. Nierengarten and A. Petitjean, *Dalton Trans.*, 2015, **44**, 14991–15005.
21 M. Bhol, R. L. Borkar, B. Shankar, S. K. Panda, M. Wolff and M. Sathiyendiran, *Inorg. Chem.*, 2023, **62**, 11554–11569.
22 J. E. Niklas, E. A. Hiti, G. R. Wilkinson, J. T. Mayhugh, J. D. Gorden and A. E. V. Gorden, *Inorg. Chim. Acta*, 2022, **529**, 120653.
23 (*a*) K. L. Flint, D. M. Huang, O. M. Linder-Patton, C. J. Sumby and F. R. Keene, *Eur. J. Inorg. Chem.*, 2022, e202200225; (*b*) U. Phukon, B. Shankar and M. Sathiyendiran, *Dalton Trans.*, 2022, **51**, 16307–16315.
24 F. Cui, S. Li, C. Jia, J. S. Mathieson, L. Cronin, X. Yang and B. Wu, *Inorg. Chem.*, 2012, **51**, 179–187.
25 S. J. Allison, D. Cooke, F. S. Davidson, P. I. P. Elliott, R. A. Faulkner, H. B. S. Griffiths, O. J. Harper, O. Hussain,

P. J. Owen-Lynch, R. M. Phillips, C. R. Rice, S. L. Shepherd and R. T. Wheelhouse, *Angew. Chem., Int. Ed.*, 2018, **57**, 9799–9804.
26 D. J. Cooke, J. M. Cross, R. V. Fennessy, L. P. Harding, C. R. Rice and C. Slater, *Chem. Commun.*, 2013, **49**, 7785–7787.
27 T. K. Ronson, H. Adams, T. Riis-Johannessen, J. C. Jeffery and M. D. Ward, *New J. Chem.*, 2006, **30**, 26–28.
28 J. Malina, M. J. Hannon and V. Brabec, *Chem. – Eur. J.*, 2015, **21**, 11189–11195.
29 M. J. Hannon and L. J. Childs, *Supramol. Chem.*, 2004, **16**, 7–22.
30 J. Mayans, M. Font-Bardia, L. Di Bari, L. Arrico, F. Zinna, G. Pescitelli and A. Escuer, *Chem. – Eur. J.*, 2018, **24**, 7653–7663.
31 N. Kelly, J. Schulz, K. Gloe, T. Doert, K. Gloe, M. Wenzel, M. Acker and J. J. Weigand, *Z. Anorg. Allg. Chem.*, 2015, **641**, 2215–2221.
32 P. Levín, D. Escudero, N. Díaz, A. Oliver, A. G. Lappin, G. Ferraudi and L. Lemus, *Inorg. Chem.*, 2020, **59**, 1660–1674.
33 L. Fabbrizzi, *J. Org. Chem.*, 2020, **85**, 12212–12226.
34 M. J. Romero, R. Carballido, L. Rodríguez-Silva, M. Maneiro, G. Zaragoza, A. M. González-Noya and R. Pedrido, *Dalton Trans.*, 2016, **45**, 16162–16165.
35 C. A. J. Hooper, L. Cardo, J. S. Craig, L. Melidis, A. Garai, R. T. Egan, V. Sadovnikova, F. Burkert, L. Male, N. J. Hodges, D. F. Browning, R. Rosas, F. Liu, F. V. Rocha, M. A. Lima, S. Liu, D. Bardelang and M. J. Hannon, *J. Am. Chem. Soc.*, 2020, **142**, 20651–20660.
36 L. Cardo, I. Nawroth, P. J. Cail, J. A. McKeating and M. J. Hannon, *Sci. Rep.*, 2018, **8**, 2–8.
37 L. J. Childs, M. Pascu, A. J. Clarke, N. W. Alcock and M. J. Hannon, *Chem. – Eur. J.*, 2004, **10**, 4291–4300.
38 P. E. Kruger, N. Martin and M. Nieuwenhuyzen, *J. Chem. Soc., Dalton Trans.*, 2001, 1966–1970.
39 F. Habib, J. Long, P. H. Lin, I. Korobkov, L. Ungur, W. Wernsdorfer, L. F. Chibotaru and M. Murugesu, *Chem. Sci.*, 2012, **3**, 2158–2164.
40 G. Novitchi, J. P. Costes, J. P. Tuchagues, L. Vendier and W. Wernsdorfer, *New J. Chem.*, 2008, **32**, 197–200.
41 S. Fernández-Fariña, I. Velo-Heleno, M. Martínez-Calvo, M. Maneiro, R. Pedrido and A. M. González-Noya, *Int. J. Mol. Sci.*, 2023, **24**, 8654.
42 G. M. Sheldrick, *Program for Scaling and Correction of Area Detector Data*, University, 1996.
43 G. M. Sheldrick, *Acta Crystallogr., Sect. C: Struct. Chem.*, 2015, **71**, 3–8.
44 I. Usón and G. M. Sheldrick, *Acta Crystallogr., Sect. D: Struct. Biol.*, 2018, **74**, 106–116.
45 C. F. Macrae, I. J. Bruno, J. A. Chisholm, P. R. Edgington, P. Mccabe, E. Pidcock, L. Rodriguez-Monge, R. Taylor, J. Van De Streek and P. A. Wood, *J. Appl. Crystallogr.*, 2008, 466–470.
46 G. Han, Y. Zhou, Y. Yao, Z. Cheng, T. Gao, H. Li and P. Yan, *Dalton Trans.*, 2020, **49**, 3312–3320.
47 G. A. Jeffrey, *An introduction to hydrogen bonding*, Oxford University Press, 1997.
48 S. H. Sumrra, A. U. Hassan, M. Imran, M. Khalid, E. U. Mughal, M. N. Zafar, M. N. Tahir, M. A. Raza and A. A. C. Braga, *Appl. Organomet. Chem.*, 2020, e5623.
49 H. Ünver, C. T. Zeyrek, B. Boyacioglu, M. Yıldız, N. Demir and A. Elmali, *J. Chem. Crystallogr.*, 2019, **49**, 232–244.
50 L. D. S. Mariano, I. M. L. Rosa, N. R. De Campos, A. C. Doriguetto, D. F. Dias, W. D. Do Pim, A. K. S. M. Valdo, F. T. Martins, M. A. Ribeiro, E. E. B. De Paula, E. F. Pedroso, H. O. Stumpf, J. Cano, F. Lloret, M. Julve and M. V. Marinho, *Cryst. Growth Des.*, 2020, **20**, 2462–2476.
51 J. Hildebrandt, N. Häfner, H. Görls, M. C. Barth, M. Dürst, I. B. Runnebaum and W. Weigand, *Int. J. Mol. Sci.*, 2022, **23**, 6669.
52 I. V. Ershova, I. V. Smolyaninov, A. S. Bogomyakov, M. V. Fedin, A. G. Starikov, A. V. Cherkasov, G. K. Fukin and A. V. Piskunov, *Dalton Trans.*, 2019, **48**, 10723–10732.
53 B. Ivanova and M. Spiteller, *J. Mol. Struct.*, 2022, **1248**, 131488.
54 S. Fernández-Fariña, I. Velo-Heleno, M. Martínez-Calvo, R. Barcia, Ò. Palacios, M. Capdevila, A. M. González-Noya and R. Pedrido, *Int. J. Mol. Sci.*, 2023, **24**, 2246.
55 J. Zhao, S. Wang and W. Zhang, *J. Chem. Crystallogr.*, 2022, **52**, 34–42.
56 P. Cucos, F. Tuna, L. Sorace, I. Matei, C. Maxim, S. Shova, R. Gheorghe, A. Caneschi, M. Hillebrand and M. Andruh, *Inorg. Chem.*, 2014, **53**, 7738–7747.
57 (*a*) M. Vázquez, A. Taglietti, D. Gatteschi, L. Sorace, C. Sangregorio, A. M. González, M. Maneiro, R. M. Pedrido and M. R. Bermejo, *Chem. Commun.*, 2003, **3**, 1840–1841; (*b*) R. A. Tigaa and A. de Bettencourt-Dias, *J. Chem. Crystallogr.*, 2017, **47**, 233–240; (*c*) C. Puigjaner, A. Portell, A. Blasco, M. Font-Bardia and O. Vallcorba, *Crystals*, 2021, **11**, 342.
58 L. Yang, D. R. Powell and R. P. Houser, *Dalton Trans.*, 2007, 955–964.